High-resolution structures of *Trypanosoma brucei* pteridine reductase ligand complexes inform on the placement of new molecular entities in the active site of a potential drug target

Alice Dawson, **Lindsay B. Tulloch**[‡], **Keri L. Barrack**, and **William N. Hunter**[*]
Division of Biological Chemistry and Drug Discovery, College of Life Sciences, University of Dundee, Dundee DD1 5EH, Scotland

Abstract

Pteridine reductase (PTR1) is a potential target for drug development against parasitic *Trypanosoma* and *Leishmania* species. These protozoa cause serious diseases for which current therapies are inadequate. High-resolution structures have been determined, using data between 1.6 and 1.1 Å resolution, of *T. brucei* PTR1 in complex with pemetrexed, trimetrexate, cyromazine and a 2,4-diaminopyrimidine derivative. The structures provide insight into the interactions formed by new molecular entities in the enzyme active site with ligands that represent lead compounds for structure-based inhibitor development and to support early-stage drug discovery.

1. Introduction

The protozoan parasites *Trypanosoma* and *Leishmania* species are the causal agents of serious diseases such as human African trypanosomiasis (HAT; sleeping sickness) and the different forms of leishmaniasis (Barrett *et al.*, 2007; Reithinger *et al.*, 2007). The drugs in current use, for example the arsenical compound called melarsoprol, are toxic, possess limited efficacy and are costly. In addition, the available treatments are being compromised by the increase in drug-resistant parasites (Croft *et al.*, 2006; Delespaux & de Koning, 2007). New drugs are therefore urgently sought and the significant advances in understanding the biology and metabolism of the protozoans holds the promise of identifying new targets for the application of structure-based inhibitor approaches to underpin early-stage drug discovery (Hunter, 2009).

One promising target is pteridine reductase (PTR1; EC 1.5.1.33), an enzyme unique to trypanosomatid parasites that supports the provision of reduced biopterins necessary for metacyclogenesis (Cunningham *et al.*, 2001) and which has been implicated in resistance to reactive oxygen and nitrogen species in *Leishmania* (Moreira *et al.*, 2009). This NADPH-dependent short-chain dehydrogenase/reductase (SDR) is a broad-spectrum pterin reductase that is able to catalyze four reductions (Nare *et al.*, 1997): biopterin to dihydrobiopterin (H_2B), H_2B to tetrahydrobiopterin (H_4B), folate to dihydrofolate (H_2F) and H_2F to tetrahydrofolate (H_4F). The last of these reductions is the same reaction as is catalyzed by dihydrofolate reductase (DHFR; EC 1.5.1.3; Blakley, 1995), a key enzyme of folate metabolism and a validated target for antifolate drugs such as methotrexate (MTX), pyrimethamine and trimethoprim (McGuire, 2003). PTR1, since it is able to reduce H_2F,

[*]Correspondence: w.n.hunter@dundee.ac.uk.
[‡]Present address: Division of Medical Sciences, Ninewells Hospital, University of Dundee, Dundee DD1 9SY, Scotland.

contributes to antifolate drug resistance by providing a bypass of DHFR inhibition (Hardy *et al.*, 1997).

We have previously identified distinct molecular scaffolds to support the design of new PTR1 inhibitors based on structural data for the *T. brucei* (*Tb*PTR1) and *L. major* (*Lm*PTR1) enzymes (Gourley *et al.*, 2001; McLuskey *et al.*, 2004; Schüttelkopf *et al.*, 2005; Dawson *et al.*, 2006; Gibson *et al.*, 2009; Mpamhanga *et al.*, 2009) and have shown that dual DHFR–PTR1 inhibition may provide a successful treatment for trypanosomatid infections (Cavazzuti *et al.*, 2008; Tulloch *et al.*, 2010). Potent DHFR inhibitors are already known and we seek to design or discover novel PTR1 inhibitors, concentrating on the enzyme from *T. brucei* (*Tb*PTR1) since this organism causes the disease with the greatest unmet medical need, HAT. We identified ligands of interest (Fig. 1) and predicted that the three largest compounds, each of which has a well defined pharmacology and proven bioavailability, would be likely to be potent inhibitors of the enzyme. These compounds carry a number of new molecular features, *e.g.* dimethoxyphenyl and trimethoxyphenyl groups, that would serve to inform about what interactions are possible in the PTR1 active site.

We now report high-resolution crystal structures of these *Tb*PTR1 ligand complexes. Cyromazine (*N*-cyclopropyl-1,3,5-triazine-2,4,6-triamine) is a cyclopropyl derivative of melamine that is used in veterinary medicine as an ectoparasiticide but with an unknown mode of action. The structure has been reported at 2.0 Å resolution previously (Tulloch *et al.*, 2010) and we now extend that to 1.1 Å resolution, revealing a level of detail not previously observed. Pemetrexed (2-{4-[2-(4-amino-2-oxo-3,5,7-triazabicyclo[4.3.0]nona-3,8,10-trien-9-yl)-ethyl]benzoyl}aminopentanedioic acid) is a folate anti-metabolite (Avendaño & Menendez, 2008) which inhibits thymidylate synthase, DHFR and glycinamide ribonucleotide formyltransferase, enzymes that are involved in both purine and pyrimidine biosynthesis. This compound is in clinical use for the treatment of lung cancer (Baldwin & Perry, 2009). Trimetrexate {5-methyl-6-[(3,4,5-trimethoxyphenyl)aminomethyl]quinazoline-2,4-diamine} is a potent DHFR inhibitor that is used in the treatment of pneumocystis pneumonia and is being investigated as an anticancer agent (Fishman, 1998; Purcell & Ettinger, 2003). Finally, there is the pyrimidine derivative 2,4-diamino-5-[2-(2,5-dimethoxyphenyl)ethyl]thieno-[2,3-*d*]-pyrimidine (PY848; Rosowsky *et al.*, 1993). To complement the structural data, K_i values were determined.

2. Materials and methods

2.1. Protein purification and storage

Recombinant *Tb*PTR1 was purified by established methods (Dawson *et al.*, 2006) and was concentrated to 22 mg ml^{-1} in 20 mM Tris–HCl pH 8.0. Aliquots were frozen in liquid nitrogen and stored at 253 K until required.

2.2. Ligand sourcing and inhibition assay

Cyromazine was a gift from Novartis Animal Health Inc. (Basel, Switzerland); the other compounds were obtained from the Center for Organic and Medicinal Chemistry, Research Triangle International (North Carolina, USA) and were used as supplied. The K_i values for these ligands were determined using a previously published method, with MTX providing a control (data not shown; Dawson *et al.*, 2006).

2.3. Crystal preparation

Crystals of *Tb*PTR1 in a binary complex with oxidized cofactor (NADP$^+$) were grown using sitting-drop vapour diffusion in drops consisting of 10 µl protein solution (6 mg ml^{-1} *Tb*PTR1, 1 mM NADP$^+$ and 1 mM DTT in 20 mM Tris–HCl pH 8.0) and 10 µl reservoir

solution (2–3 M sodium acetate and 20–100 mM sodium citrate pH 4.5). The conditions were stored at room temperature (approximately 291 K) and monoclinic plate-like crystals formed overnight and grew to 2 mm in length over several days. The ligands pemetrexed, trimetrexate and PY848 (2.5 µl at a concentration of 10 mM) were added to drops containing one or two large crystals and the samples were left for 24 h. The final concentration of the ligand was approximately 1 mM.

Crystals of the *Tb*PTR1–NADPH–cyromazin complex were grown in hanging drops consisting of 1.5 µl protein solution [*Tb*PTR1 at 6–10 mg ml^{-1}, 1 mM NADPH, 3 mM cyromazin, 1%(*v/v*) DMSO and 20 mM DTT] and an equal volume of reservoir solution (1.5–3 M sodium acetate, 10–50 mM sodium citrate in the pH range 4.5–6.0) at approximately 291 K. The largest crystals grew to approximately $0.5 \times 0.3 \times 0.1$ mm over a few days. Crystals grown in excess of 2.6 M sodium acetate were flash-cooled in liquid nitrogen directly from the mother liquor. Those obtained at a lower salt concentration were cryoprotected with 3 M sodium acetate prior to flash-cooling.

2.4. X-ray data collection and structure determination

X-ray data were collected at the European Synchrotron Radiation Facility (ESRF), Grenoble, France on beamline ID14-4 for the pemetrexed, trimetrexate and PY848 complexes and on beamline ID29 for the cyromazine complex. Both beamlines were equipped with an ADSC Q315 CCD detector. X-ray images from the pemetrexed and trimetrexate complexes were integrated and scaled with *XDS* and *XSCALE* (Kabsch, 2010). *MOSFLM* (Leslie, 2006) and *SCALA* (Evans, 2006) were used to process the data from the PY848 and cyromazine complexes. All of the complex structures are isomorphous, with four subunits in the asymmetric unit, and refinement started using a tetramer of *Tb*PTR1 (Dawson *et al.*, 2006; PDB code 2c7v) for rigid-body refinement in *REFMAC5* (Murshudov *et al.*, 1999). Several rounds of restrained refinement, still using *REFMAC5*, were carried out together with inspection of electron-density and difference density Fourier maps (Collaborative Computational Project, Number 4, 1994), model manipulation and identification of multiple conformers, water molecules, ions and ligands with *Coot* (Emsley & Cowtan, 2004) using similar protocols to those previously published (Tulloch *et al.*, 2010). Noncrystallographic symmetry restraints were not used at any stage in these analyses. In all four cases, the initial refinement calculations included isotropic thermal parameters and these were subsequently changed to anisotropic thermal parameters for the cyromazine, pemetrexed and trimetrexate complexes. With the high-resolution diffraction data available for the cyromazine and pemetrexed complexes, it was decided to switch to the refinement program *SHELX* (Sheldrick, 2008). C—H and main-chain amide N—H H atoms were included in the final stages of refinement with anisotropic thermal parameters refined for all non-H atoms using appropriate restraints. Figures were generated with *PyMOL* (DeLano, 2002). Crystallographic statistics are given in Table 1.

3. Results and discussion

3.1. *Tb*PTR1 structure and organization of the active site

PTR1 is a tetrameric SDR with a single α/β-domain subunit that is a Rossmann-fold repeat (Gourley *et al.*, 2001; Fig. 2). An elongated active site is primarily formed by a single subunit, with one end blocked by the C-terminus of a partner subunit. A loop formed by residues 207–215 in *Tb*PTR1 forms part of the active site and since it interacts with substrates this is called the substrate-binding loop (Tulloch *et al.*, 2010; Fig. 2). The enzyme structure is well conserved in *Tb*PTR1–ligand complexes (Tulloch *et al.*, 2010) and this observation also applies to the four complexes now reported. For example, the C$^\alpha$ atoms of the four subunits in the *Tb*PTR1–pemetrexed complex overlay with an r.m.s.d. in the range

0.17–0.22 Å. Given the high degree of noncrystallographic symmetry and the conservation of the interactions formed in the four active sites in the asymmetric unit, it is only necessary to detail one and subunit *A* has been chosen arbitrarily. Some structural variations are observed in the *Tb*PTR1–cyromazine structure involving the propyl substitutent and this is detailed below.

The binding of the cofactor is essential to create both the catalytic centre and the substrate-binding site and explains why PTR1 displays an ordered sequential mechanism with first NADPH binding and then substrate. The product, a reduced pterin, is released followed by NADP$^+$ before another reduction can occur (Luba *et al.*, 1998). The pterin substrates and inhibitors bind in a π-sandwich between the nicotinamide and Phe97 and also interact with the β-phosphate group. Here, the ribose and a phosphate of the cofactor, Arg14, Ser95, Asn127, Lys178 and two catalytically important residues, Asp161 and Tyr174, are positioned to organize the active site and interact with ligands (Fig. 3).

A series of hydrogen bonds help to position key functional groups to interact with ligands. On one side of the active site, Lys178 NZ donates hydrogen bonds to the nicotinamide ribose O2$'$ and O3$'$ groups and to Asn127 OD1. Asn127 ND2 donates two hydrogen bonds to the carbonyl groups of Ala96 and Leu123 (data not shown) and so the side chain is well fixed. Since Asn127 OD1 then accepts a hydrogen bond from Ser96 OG, the serine hydroxyl group is aligned to function as a hydrogen-bond acceptor in the active site. The ribose O2$'$ is aligned to function as a hydrogen-bond donor. Nearby, Tyr174 OH is within hydrogen-bonding distance of Asp161 OD2. On the other side of the active site, the Arg14 guanidinium group helps to organize the start of the substrate-binding loop that is adjacent to the nicotinamide by donating hydrogen bonds to the main-chain carbonyl groups of Leu208 and Leu209 (not shown). In addition, Arg14 also forms hydrogen bonds to both the α-phosphate and β-phosphate groups of NADPH. The nicotinamide N7 donates hydrogen bonds to the carbonyl group of Leu208 and the α-phosphate O2. These interactions contribute to the placement of the β-phosphate O2 to accept hydrogen bonds donated by ligands.

3.2. The *Tb*PTR1–NADPH–cyromazine complex

The structure of the complex of *Tb*PTR1–NADP$^+$ and cyromazine ($K_i > 35$ μ*M*) has previously been reported at 2.0 Å resolution (Tulloch *et al.*, 2010) and this is now extended to 1.1 Å by virtue of being able to grow more ordered larger crystals combined with the use of an undulator as opposed to a bending-magnet beamline for diffraction measurements. The placement of the ligand in the active site and key interactions are depicted in Fig. 4. The use of NADPH and a higher concentration of DTT appears to have helped the crystallization process. In the lower resolution structure Cys168 at one side of the active site has been oxidized to sulfenic acid. In this higher resolution structure the cysteine is present as a thiol, but nearby is an oxidized circular DTT that adopts two conformations. This DTT occupies what in other structures is a water-filled cavity. We see no difference in the structure of or the interactions with the different states of the cofactor.

The triazine group binds as previously reported. The proximity of the NADPH β-phosphate O2 to N1 suggests that the ligand is protonated here, as observed when the archetypal antifolate MTX binds DHFR (Bennett *et al.*, 2006) or PTR1 (Gourley *et al.*, 2001). The amino N2 group donates a hydrogen bond to Ser95 OG and the geometry at this high resolution is consistent with a second hydrogen bond: a bifurcated interaction (Leonard *et al.*, 1995) with the Ser95 main-chain carbonyl and the β-phosphate O2. N3 accepts a hydrogen bond from the ribose O2$'$ and N4 donates one to Tyr174 OH. N7 participates in a water-mediated interaction with O2 of the β-phosphate. The position of the propyl groups varies between the four subunits. In subunit *A* only one orientation is observed, with van der

Waals interactions formed to Arg14, Phe97 and Pro210. In subunits *B*, *C* and *D* the propyl group is disordered over two positions: in addition to the subunit *A*-type orientation, the propyl group is also observed pointing away from the active-site pocket. Refinement indicated relative occupancies of 0.33:0.67 for these two orientations (data not shown). In the lower resolution structure only one orientation of the propyl group, corresponding to that observed in subunit *A*, was modelled (Tulloch *et al.*, 2010).

3.3. The TbPTR1–NADP⁺–pemetrexed complex

Pemetrexed (K_i of ~30 nM) binds adopting a substrate-like orientation with the pyrimidine positioned in the same way as observed in the complexes with biopterin, H_2B and H_2F (Fig. 5; Gourley *et al.*, 2001; Tulloch *et al.*, 2010). N1 donates a hydrogen bond to the β-phosphate O2, and N2 forms hydrogen bonds to Ser95, including a bifurcated interaction with the β-phosphate O2. N3 and N9 accept and donate hydrogen bonds to the ribose O2′ and Tyr174 OH, respectively. O6 accepts hydrogen bonds donated from Arg14 and a water molecule, which also interacts with the β-phosphate O2. The benzyl group and linking region form van der Waals interactions with Phe197, Val206, Leu209, Pro210, Met213 (not shown) and Trp221. The glutamate tail is directed out of the active site, is solvent-accessible and adopts two conformations. In one conformation, hydrogen bonds are formed to His267 from a partner subunit in the tetramer and to the main-chain amide of Met169 (data not shown). The other conformation allows van der Waals interactions with Pro99 (data not shown).

3.4. The *Tb*PTR1–NADP⁺–trimetrexate complex

Trimetrexate (K_i of ~70 nM) binds with the quinazoline adopting an orientation similar to that observed for the pterin of MTX (Fig. 6; Gourley *et al.*, 2001). N1 accepts a hydrogen bond from the ribose O2′ and N2 forms the same hydrogen-bonding interactions to Ser95 and the β-phosphate as seen in the other two complexes. N4 donates a hydrogen bond to Tyr174 OH and to a water molecule that also interacts with Asp161. Tyr174 OH and Asp161 OD2 share a hydrogen bond donated by the hydroxyl group. N1 is the site of protonation that allows interaction with the β-phosphate O2. The methyl substituent at C7 is directed into the solvent-filled cavity. The amide in the linker region between the quinazoline and the trimethoxy-substituted phenyl group is directed towards the solvent-filled cavity and donates a hydrogen bond to a well ordered water molecule. This water then forms a hydrogen bond to the thiol group of Cys168. The trimethoxyphenyl group makes van der Waals interactions with Cys168, Phe171 (not shown), Leu209, Pro210, Met213 (not shown) and Trp221. The methoxy groups are all exposed to solvent and interactions with ordered water molecules are observed.

3.5. The *Tb*PTR1–NADP⁺–PY848 complex

PY848 (K_i of approximately 70 nM) binds in a similar orientation to that seen for pemetrexed despite the difference of the N6 hydrogen-bond-donating amino group compared with the hydrogen-bond-accepting O6 of the latter (Fig. 1). N1, N2 and N3 form similar interactions as noted for cyromazine and pemetrexed (Fig. 7). N6, like N7 of cyromazine, forms a water-mediated link to the β-phosphate O2. S9 accepts hydrogen bonds donated from Tyr178 OH and water that in turn contribute to a network of hydrogen-bonded solvent molecules near Asp161. The dimethoxyphenyl group forms van der Waals interactions with Phe97, Cys168, Leu209, Pro210 and Trp221. One of the methoxy groups is tucked down near Val206; the other is directed out of the active site and is solvent-accessible.

Previous structures of PTR1–ligand complexes have revealed that the orientation of the substrate/product pteridines is distinct from that of compounds such as MTX, which is

flipped 180° to place the chemical pattern NH_2:N:NH_2, as exemplified by N2–N1–N6 of trimetrexate (Figs. 1 and 6), directed towards the Ser95, ribose O2′ and Tyr174 part of the active site. Compound PY848, in either the substrate-like or MTX-like orientation, would be able to interact with the same number of hydrogen-bond contributions between the ligand and PTR1–NADPH. The compound adopts the substrate-like orientation, probably owing to the steric clash that would result between the dimethoxyphenyl group and side chains around the active site.

4. Concluding remarks

Accurate high-resolution crystal structures of four *Tb*PTR1–ligand complexes have been determined and reveal molecular details that have not previously been observed. Common to all four structures is a matching of hydrogen-bonding capacity between the ligands and the active site, in particular forming such interactions between the ligands and the cofactor, Ser95 and Tyr174. Also shared by the four ligands is the placement of the major ring systems between Phe97 and the nicotinamide. Three of the ligands, with the exception being cyromazine, have pronounced van der Waals interactions on one side of the active site. A degree of conformational pliability exists for the propyl substituent of cyromazine, the weakest binding inhibitor of the four, and the glutamate tail of pemetrexed and suggests areas of the active site where space is available to fill by modification of known inhibitor frameworks. The trimethoxyphenyl and dimethoxyphenyl groups of trimetrexate and PY848, respectively, are well ordered and form stabilizing van der Waals forces with residues at the periphery of the active site, in particular with Trp221. PY848 binds placing the NH_2:N:NH_2 pattern directed towards the β-phosphate group of the cofactor rather than, as expected, towards the Tyr174 side chain and ribose. Such an orientation prevents the steric clash of the dimethoxyphenyl group with the substrate-binding loop that would be observed with the MTX-like binding as displayed by trimetrexate. These two compounds (trimetrexate and PY848) are potent inhibitors of *Tb*PTR1 and both display a K_i of approximately 70 n*M* irrespective of the different orientation of the ring systems that bind between Phe97 and the nicotinamide. Trimetrexate adopts the MTX-like mode of binding, but the K_i is improved from 140 n*M* for MTX to 70 n*M*. The presence of the trimethoxy group on trimetrexate and the increased van der Waals contacts with a hydrophobic part of the active site created by Leu209, Pro210 and Trp221 in particular may contribute to this enhanced inhibition. The complex structure certainly suggests that this substituent might be incorporated into additional scaffolds to investigate exactly what it might contribute to binding. With a K_i of around 30 n*M*, pemetrexate registers as a highly potent inhibitor of *Tb*PTR1. In common with those of trimetrexate and PY848, the pemetrexate complex suggests that van der Waals interactions with a hydrophobic part of the active site are important for strong binding. The new structural models that result from our study now provide highly accurate templates that can be exploited by molecular-design approaches seeking to modify known inhibitor frameworks to incorporate new interactions in the *Tb*PTR1 active site.

Acknowledgments

References

Avendaño, C.; Menendez, JC. Medicinal Chemistry of Anticancer Drugs. Elsevier; Amsterdam: 2008. p. 37

Baldwin CM, Perry CM. Drugs. 2009; 69:2279–2302. [PubMed: 19852529]

Barrett MP, Boykin DW, Brun R, Tidwell RR. Br. J. Pharmacol. 2007; 152:1155–1171. [PubMed: 17618313]

Bennett B, Langan P, Coates L, Mustyakimov M, Schoenborn B, Howell EE, Dealwis C. Proc. Natl Acad. Sci. USA. 2006; 103:18493–18498. [PubMed: 17130456]

Blakley RL. Adv. Enzymol. Relat. Areas Mol. Biol. 1995; 70:23–102. [PubMed: 8638484]

Cavazzuti A, Paglietti G, Hunter WN, Gamarro F, Piras S, Loriga M, Allecca S, Corona P, McLuskey K, Tulloch L, Gibellini F, Ferrari S, Costi MP. Proc. Natl Acad. Sci. USA. 2008; 105:1448–1453. [PubMed: 18245389]

Collaborative Computational Project. Acta Cryst. 1994; D50:760–763. Number 4.

Croft SL, Sundar S, Fairlamb AH. Clin. Microbiol. Rev. 2006; 19:111–126. [PubMed: 16418526]

Cruickshank DWJ. Acta Cryst. 1999; D55:583–601.

Cunningham ML, Titus RG, Turco SJ, Beverley SM. Science. 2001; 292:285–287. [PubMed: 11303103]

Dawson A, Gibellini F, Sienkiewicz N, Tulloch LB, Fyfe PK, McLuskey K, Fairlamb AH, Hunter WN. Mol. Microbiol. 2006; 61:1457–1468. [PubMed: 16968221]

DeLano WL. PyMOL. 2002 http://www.pymol.org.

Delespaux V, de Koning HP. Drug Resist. Updates. 2007; 10:30–50.

Emsley P, Cowtan K. Acta Cryst. 2004; D60:2126–2132.

Evans P. Acta Cryst. 2006; D62:72–82.

Fishman JA. Antimicrob. Agents Chemother. 1998; 42:1309–1314. [PubMed: 9624465]

Gibson CL, Huggan JK, Kennedy A, Kiefer L, Lee JH, Suckling CJ, Clements C, Harvey AL, Hunter WN, Tulloch LB. Org. Biomol. Chem. 2009; 7:1829–1842. [PubMed: 19590778]

Gourley DG, Schüttelkopf AW, Leonard GA, Luba J, Hardy LW, Beverley SM, Hunter WN. Nature Struct. Biol. 2001; 8:521–525. [PubMed: 11373620]

Hardy LW, Matthews W, Nare B, Beverley SM. Exp. Parasitol. 1997; 87:158–170. [PubMed: 9398595]

Hunter WN. J. Biol. Chem. 2009; 284:11749–11753. [PubMed: 19103598]

Kabsch W. Acta Cryst. 2010; D66:125–132.

Leonard GA, McAuley-Hecht K, Brown T, Hunter WN. Acta Cryst. 1995; D51:136–139.

Leslie AGW. Acta Cryst. 2006; D62:48–57.

Luba J, Nare B, Liang P-H, Anderson KS, Beverley SM, Hardy LW. Biochemistry. 1998; 37:4093–4104. [PubMed: 9521731]

McGuire JJ. Curr. Pharm. Des. 2003; 9:2593–2613. [PubMed: 14529544]

McLuskey K, Gibellini F, Carvalho P, Avery MA, Hunter WN. Acta Cryst. 2004; D60:1780–1785.

Moreira W, Leblanc E, Ouellette M. Free Radic. Biol. Med. 2009; 46:367–375. [PubMed: 19022374]

Mpamhanga CP, Spinks D, Tulloch LB, Shanks EJ, Robinson DA, Collie IT, Fairlamb AH, Wyatt PG, Frearson JA, Hunter WN, Gilbert IH, Brenk R. J. Med. Chem. 2009; 52:4454–4465. [PubMed: 19527033]

Murshudov GN, Vagin AA, Lebedev A, Wilson KS, Dodson EJ. Acta Cryst. 1999; D55:247–255.

Nare B, Hardy LW, Beverley SM. J. Biol. Chem. 1997; 272:13883–13891. [PubMed: 9153248]

Purcell WT, Ettinger DS. Curr. Oncol. Rep. 2003; 5:114–125. [PubMed: 12583828]

Reithinger R, Dujardin JC, Louzir H, Pirmez C, Alexander B, Brooker S. Lancet Infect. Dis. 2007; 7:581–596. [PubMed: 17714672]

Rosowsky A, Mota CE, Wright JE, Freisheim JH, Heusner JJ, McCormack JJ, Queener SF. J. Med. Chem. 1993; 36:3103–3112. [PubMed: 8230096]

Sheldrick GM. Acta Cryst. 2008; A64:112–122.

Schüttelkopf AW, Hardy LW, Beverley SM, Hunter WN. J. Mol. Biol. 2005; 352:105–116. [PubMed: 16055151]

Tulloch LB, Martini VP, Iulek J, Huggan JK, Lee JH, Gibson CL, Smith TK, Suckling CJ, Hunter WN. J. Med. Chem. 2010; 53:221–229. [PubMed: 19916554]
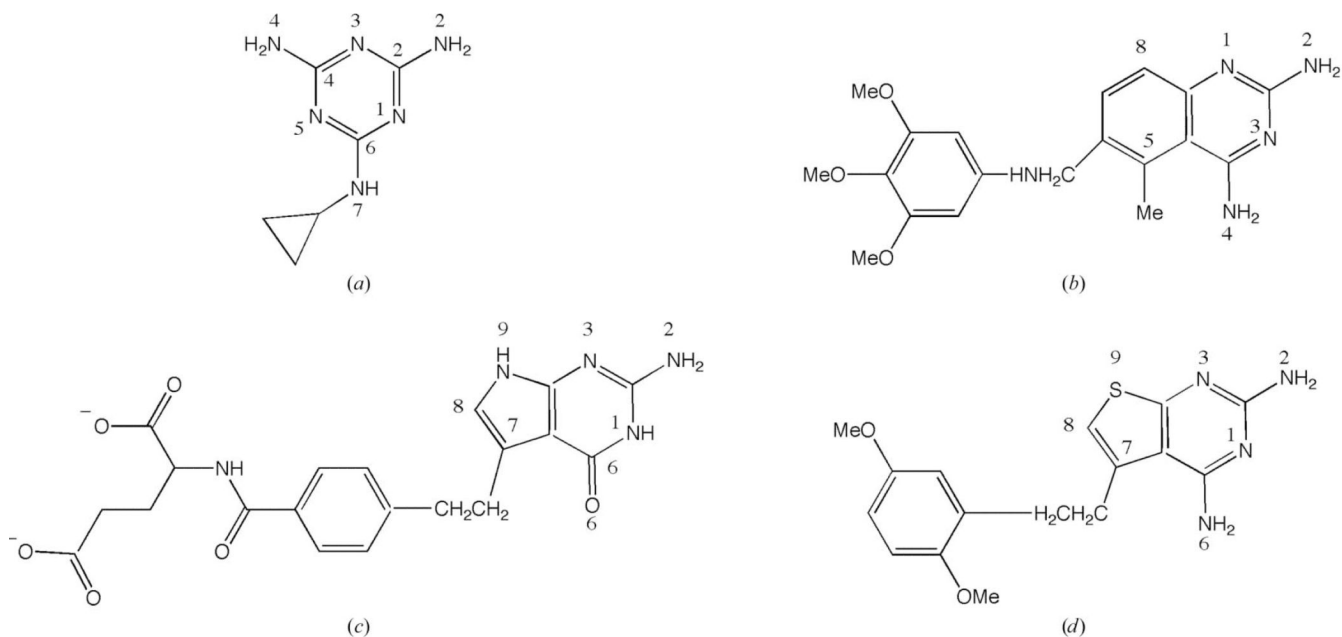
Figure 1.
The chemical structures and atomic numbering of the four ligands. (*a*) Cyromazine, *N*-cyclopropyl-1,3,5-triazine-2,4,6-triamine. (*b*) Trimetrexate, 5-methyl-6-[(3,4,5-trimethoxyphenyl)aminomethyl]quinazoline-2,4-diamine. (*c*) Pemetrexed, 2-{4-[2-(4-amino-2-oxo-3,5,7-triazabicyclo[4.3.0]nona-3,8,10-trien-9-yl)ethyl]benzoyl}aminopentanedioic acid. (*d*) PY848, 2,4-diamino-5-[2-(2,5-dimethoxyphenyl)ethyl]thieno[2,3-*d*]-pyrimidine.
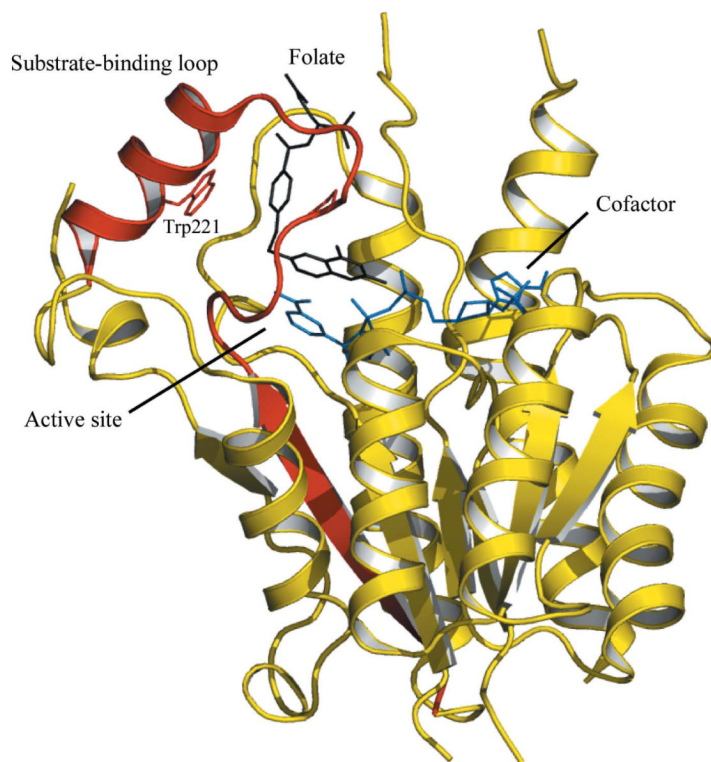
Figure 2.
Ribbon diagram of the *Tb*PTR1 subunit architecture and the position of the active site. The $\beta6$–loop–$\alpha6$ segment is coloured red. The cofactor is depicted as blue sticks and the substrate, folate, as black sticks. The side chain of Trp221, on the edge of the active site, is shown as red sticks. Figs. 2 and 3 were derived using PDB entry 3bmc (Tulloch *et al.*, 2010).
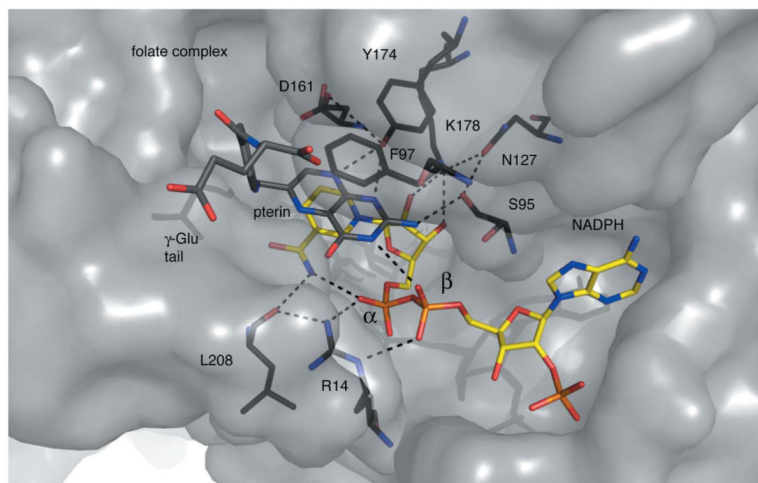
Figure 3.
Residues and hydrogen bonds organize the *Tb*PTR1 active site. PTR1 is shown as a grey semi-transparent van der Waals surface. Specific residues are coloured: C, black; N, blue; O, red. NADPH is depicted with C atoms coloured yellow and P atoms orange and folate with C atoms in dark grey. Dashed lines represent potential hydrogen-bonding interactions.
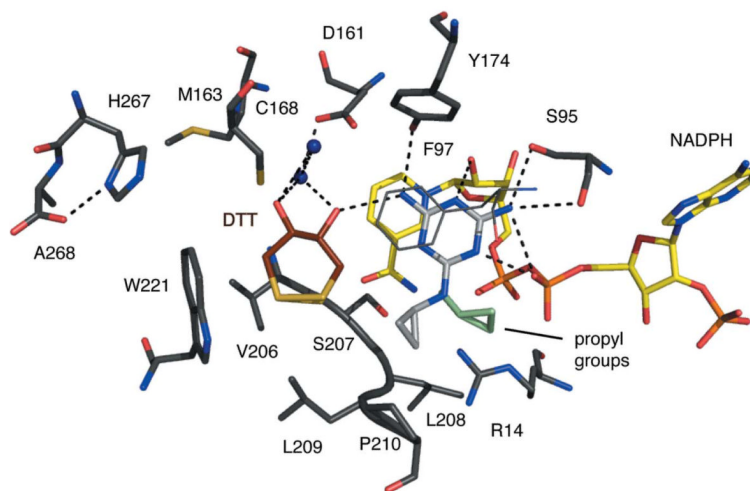
Figure 4.

*Tb*PTR1 in complex with cyromazine. Atomic positions are coloured: N, blue; O, red; P, orange; S, dark yellow; C of PTR1, dark grey; C of cofactor, yellow; C of DTT, brown. The C atoms of cyromazine are shown in light grey but for the second conformer of the propyl group they are shown in light green. The side chain of Phe97 is directly over the cyromazine-binding position and for clarity is shown in thin dark grey lines. Potential hydrogen bonds are depicted as dashed lines and water molecules are shown as blue spheres.
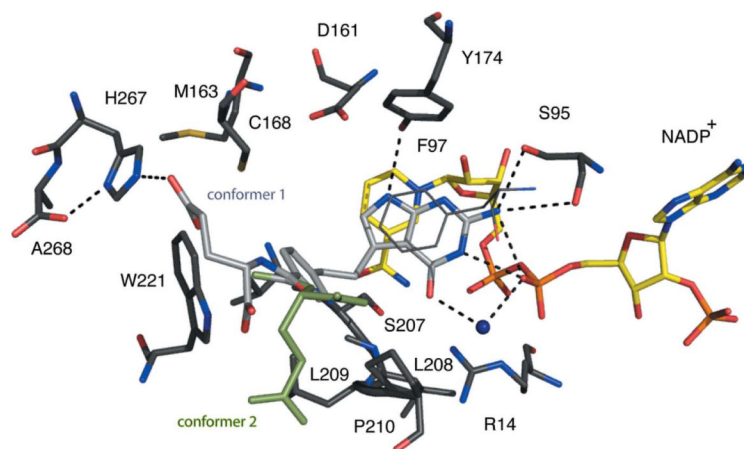
Figure 5.

*Tb*PTR1 in complex with pemetrexed. The same colour scheme as Fig. 4 is adopted, with C atoms of the pemetrexed coloured light grey. In addition, the C atoms of conformer 1 of the glutamate tail are shown in light grey and those of conformer 2 are shown in light green.
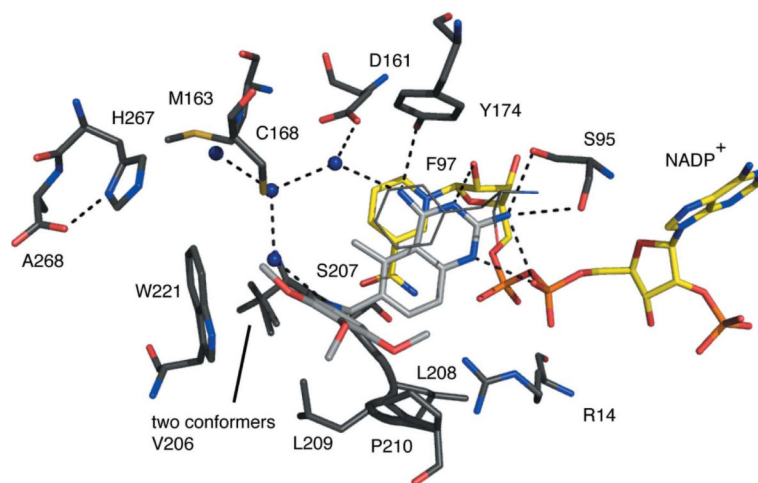
Figure 6.
*Tb*PTR1 in complex with trimetrexate. The same colour scheme as Fig. 4 is adopted, with C atoms of the trimetrexate coloured light grey.
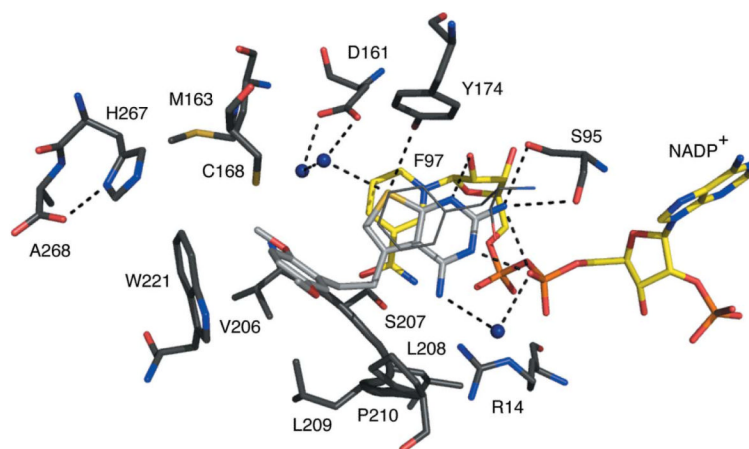
Figure 7.
*Tb*PTR1 in complex with PY848. The same colour scheme as Fig. 4 is adopted, with C atoms of PY848 coloured light grey.

Table 1

Crystallographic statistics. Values in parentheses are for the highest resolution shell.

Ligand	Cyromazin	Pemetrexed	PY848	Trimetrexate
PDB code	3×9n	2×9g	3mcv	2×9v
Resolution range (Å)	45.13–1.15	41.80–1.10	44.90–1.70	31.05–1.30
Space group	$P2_1$	$P2_1$	$P2_1$	$P2_1$
Unit-cell parameters				
a (Å)	74.50	74.72	74.50	74.56
b (Å)	90.00	90.57	89.82	90.71
c (Å)	82.40	83.58	82.26	82.46
β (°)	115.0	115.6	115.5	115.7
Scaling				
No. of measurements	1358806	1704349	598600	1337387
No. of unique measurements	385887	396089	105672	239044
Multiplicity	3.4 (3.2)	4.3 (3.8)	5.7 (5.5)	5.6 (5.5)
Completeness (%)	96.2 (93.7)	98.7 (96.7)	98.5 (97.4)	98.8 (98.6)
$\langle I/\sigma(I)\rangle$	15.3 (4.3)	15.6 (4.4)	9.8 (2.4)	15.9 (4.6)
$R_{\mathrm{merge}}{}^{\dagger}$ (%)	6.1 (23.0)	5.2 (29.2)	6.1 (30.8)	8.7 (40.1)
Refinement				
$R_{\mathrm{work}}{}^{\ddagger}$ (%)/No. of reflections	12.58/368821	12.06/378868	13.5/100335	12.1/226950
$R_{\mathrm{free}}{}^{\S}$ (%)/No. of reflections	15.26/16882	14.68/17155	16.7/5310	14.8/12094
R.m.s.d. bond lengths (Å)	0.016	0.014	0.012	0.010
R.m.s.d. bond angles (°)	2.24	2.12	1.454	1.405
DPI¶	0.03	0.04	0.09	0.04
Ramachandran plot analysis				
Favoured (%)	96.8	96.5	96.5	96.5
Outliers (%)	0.0	0.0	0.0	0.0
Model				
Total amino acids	992	1002	1000	1000
Overall B factor (Å^2)	15.4	15.8	10.1	15.3
Residues in subunit A	248	251	251	250
Residues in subunit B	248	250	251	251
Residues in subunit C	249	252	248	249
Residues in subunit D	247	249	250	250
B factor, subunit A (Å^2)	11.5	14.8	12.0	11.9
B factor, subunit B (Å^2)	12.5	13.4	12.1	11.8
B factor, subunit C (Å^2)	12.8	14.9	13.1	12.8
B factor, subunit D (Å^2)	12.6	14.3	13.0	12.8
Additional groups				
Solvent				
No.	1382	1372	793	1202

Ligand	Cyromazin	Pemetrexed	PY848	Trimetrexate
Average B factor (Å^2)	32.4	32.2	24.6	34.9
NADP+				
B factor, subunit A (Å^2)	7.4	9.1	8.8	8.6
B factor, subunit B (Å^2)	9.0	7.7	9.0	8.4
B factor, subunit C (Å^2)	8.4	7.9	11.6	8.5
B factor, subunit D (Å^2)	9.2	8.5	10.2	9.8
Ligand				
B factor, subunit A (Å^2)	9.8	14.2	14.4	16.5
B factor, subunit B (Å^2)	22.3	17.7	18.8	13.4
B factor, subunit C (Å^2)	21.8	18.2	19.4	15.3
B factor, subunit D (Å^2)	23.7	19.2	19.5	16.7
DTT				
B factor, subunit A (Å^2)	26.1	—	—	—
B factor, subunit B (Å^2)	33.2	—	—	—
B factor, subunit C (Å^2)	31.7	—	—	34.1
B factor, subunit D (Å^2)	20.8	—	—	—
Acetate				
No.	1	1	4	6
B factor (Å^2)	12.4	13.3	21.8	19.7
Na+				
No.	2			
B factor (Å^2)	29.1			

[†] $R_{\mathrm{merge}} = \Sigma_{hkl}\Sigma_i |I_i(hkl) - \langle I(hkl)\rangle| / \Sigma_{hkl}\Sigma_i I_i(hkl)$, where $I_i(hkl)$ is the intensity of the ith measurement of reflection hkl and $\langle I(hkl)\rangle$ is the mean value of $I_i(hkl)$ for all i measurements.

[‡] $R_{\mathrm{work}} = \Sigma_{hkl} ||F_{\mathrm{obs}}| - |F_{\mathrm{calc}}|| / \Sigma_{hkl} |F_{\mathrm{obs}}|$, where F_{obs} is the observed structure-factor amplitude and F_{calc} is the structure-factor amplitude calculated from the model.

[§] R_{free} is the same as R_{work} except calculated with a 5% subset of data that were excluded from refinement calculations.

[¶] Diffraction-component precision index (Cruickshank, 1999).